Noise-Reduced 3D Organ Modeling from CT Images Using Median Filtering for Anatomical Preservation in Medical 3D Printing

Phichitphon Chotikunnan [1], Rawiphon Chotikunnan [2], Tasawan Puttasakul [3*], Wanida Khotakham [4], Pariwat Imura [5], Jaroonrut Prinyakupt [6], Nuntachai Thongpance [7], Anuchart Srisiriwat [8*]
[1, 2, 3, 4, 5, 6, 7] College of Biomedical Engineering, Rangsit University, Pathum Thani, Thailand
[8] Department of Electrical Engineering, Pathumwan Institute of Technology, Bangkok, Thailand
Email: [1] phichitphon.c@rsu.ac.th, [2] rawiphon.c@rsu.ac.th, [3] tasawan.p@rsu.ac.th, [4] wanida.k@rsu.ac.th, [5] pariwat.i@rsu.ac.th, [6] jaroonrut.p@rsu.ac.th, [7] nuntachai.t@rsu.ac.th, [8] anuchart@pit.ac.th
*Corresponding Author

***Abstract*—This study offers a systematic approach to improving the reconstruction of three-dimensional anatomical models from CT imaging data. The main difficulty tackled is the maintenance of internal bone features during denoising, essential for producing clinically relevant models. A nonlinear filtering strategy was implemented, utilizing a 3×3 median filter alongside manual refinement to eliminate salt-and-pepper noise while preserving anatomical information. The study presents a reproducible image-processing pipeline that improves structural clarity and enables material-efficient 3D printing while preserving internal bone integrity. A publicly available dataset including 813 anonymized chest CT scans (512×512 pixels, 16-bit grayscale) from Zenodo was employed. Preprocessing included grayscale normalization, brightness adjustment, and the application of median filters with kernel sizes from 3×3 to 9×9, followed by artifact removal using FlashPrint software before STL conversion. The 3×3 median filter achieved an excellent balance between noise reduction and anatomical clarity, outperforming mean filtering and larger kernels in maintaining edge detail. Although statistical evaluation was not conducted, visual analysis validated an 18.07 percent decrease in print time and a 17.88 percent reduction in filament consumption. The technology exhibited actual efficacy in generating high-quality anatomical models. Future endeavors will incorporate automated segmentation and sophisticated denoising methodologies to enhance applicability in surgical simulation, clinical education, and personalized healthcare planning.**

Keywords—Median Filtering; Medical Image Processing; STL File Generation; DICOM.

I. INTRODUCTION

Advancements in three-dimensional (3D) printing have revolutionized healthcare by facilitating the creation of patient-specific organ models for surgery planning, medical teaching, and patient communication [1], [2]. Computed tomography (CT) is crucial for obtaining high-resolution anatomical information [3]-[7]. CT images often exhibit salt-and-pepper noise, a form of random impulse noise marked by intermittent high-contrast pixels. If not treated, such noise can hide intricate anatomical boundaries, including vascular structures and organ interfaces, thereby diminishing the accuracy of 3D reconstruction for therapeutic and educational applications [8]-[10].

Conventional denoising methods may unintentionally obscure edges or eliminate minor tissue variations essential for diagnostic accuracy. Recent work on advanced preprocessing methods and convolutional neural networks has explored approaches to improve image clarity while maintaining structural integrity [11]-[16].

Numerous studies have demonstrated that effective image filtering is crucial for dependable picture-based applications in agriculture [17], medical diagnostics [18]-[20], facial recognition [21], robot-assisted perception and object segmentation in robotics [22]-[26], and healthcare [27]-[31]. Deep learning methodologies, including convolutional neural networks (CNNs) and ResNet-based architectures, are being widely utilized and have shown effectiveness in chest disease diagnosis, skin lesion classification, and semantic segmentation within both medical and industrial domains [32]-[44]. Nonetheless, preprocessing remains crucial, as noise reduction enhances feature clarity and improves the reliability of downstream tasks, including diagnosis and 3D reconstruction [45]-[50]. In surgical planning and patient-specific anatomical modeling, minimizing noise is essential to avoid misinterpretation of critical structures and to improve the 3D printing process [51], [52].

This study proposes the implementation of a median filter, a recognized non-linear filtering method that mitigates salt-and-pepper noise while preserving critical anatomical characteristics. Median filtering offers a straightforward and effective method that preserves sufficient anatomical fidelity in contrast to more intricate techniques such as bilateral filtering or anisotropic diffusion, which frequently necessitate parameter adjustment and increased computational resources. This work is unique in minimizing internal structural loss usually associated with high-threshold segmentation and in efficiently removing noise artifacts that may compromise the 3D model. Particularly in osseous tissue, this approach helps to maintain internal density, thereby allowing precise physical modeling. The organ or region of interest is delineated using thresholding and an erasing function in anatomical modeling software during post-processing.

This study meticulously assesses and compares several median filter kernel sizes (3×3, 5×5, 7×7, and 9×9) to

determine the best balance between noise reduction and feature preservation [53]-[61]. Median filtering is prioritized in this work due to its simplicity and consistent performance in retaining edge clarity with minimal parameter adjustment, despite the availability of more advanced denoising methods. The resulting 3D model is refined and printable, with potential utility in supporting medical professionals in diagnosis, surgical planning, and patient communication [62]-[66].

The growing accessibility of sophisticated image-processing methods and open-source imaging datasets has enabled wider applicability across other fields. This research concentrates on medical imaging and anatomical modeling, although certain publications in [67]-[77] emphasize applications in agriculture and robotics. The extensive applications demonstrate the adaptability of filtering procedures, although the current study emphasizes the clinical significance of generating rapid, accurate, and cost-effective anatomical models from CT data.

The main contribution of this study is a reproducible and efficient CT image filtering and modeling framework that reduces salt-and-pepper noise, preserves internal bone structure, and enables the generation of anatomically detailed 3D-printed models that may potentially support future applications in clinical planning, education, and simulation. The structure of this research is as follows. Section II offers the research technique, including segmentation of CT images, thresholding, and filtering techniques. Section III reviews the experimental results and assesses the efficiency of the proposed approach in terms of noise attenuation and 3D reconstruction quality. The study concludes in Section IV, which also provides future research directions.

II. RESEARCH METHOD

This work introduces a comprehensive image-processing pipeline that is designed to improve the quality of CT scans for the purpose of three-dimensional organ modeling and medical 3D printing. The process depicted in Fig. 1 involves a number of phases, such as dataset acquisition, preprocessing, filtering, segmentation, model refinement, and the fabrication of physical 3D models. A comparative assessment across four median filter kernel sizes (3×3, 5×5, 7×7, and 9×9) was conducted, focusing on visual evaluation of edge preservation and noise suppression. Median filtering using a 3×3 kernel size is highlighted for reducing salt-and-pepper noise while keeping important anatomical details needed for 3D reconstruction.

The procedure starts with dataset acquisition from a publicly available Zenodo repository [78]. The dataset consists of 813 anonymized DICOM slices, each with a size of 512×512 pixels and a 16-bit grayscale depth, obtained by helical CT scanning. These images were selected to represent clinically relevant spatial resolution and contrast fidelity. It is important to note that pixel-based evaluation was adopted, as the DICOM files lacked physical metadata such as PixelSpacing and SliceThickness.

In the preprocessing step using MATLAB R2024b, Hounsfield Unit (HU) values were made consistent, and the brightness was adjusted to ensure uniform contrast across all slices. The main aim was to guarantee compatibility with medical imaging software and filtration tools.

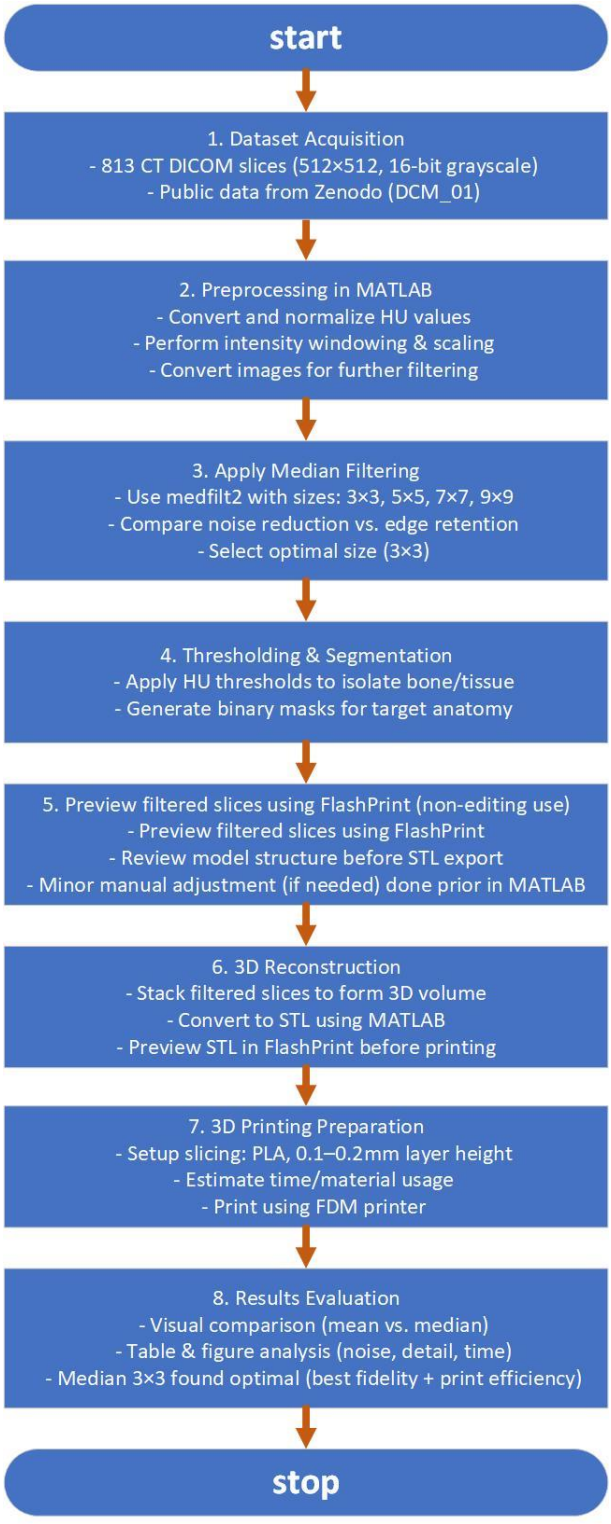

Fig. 1. Flowchart of the proposed 3D medical modeling pipeline using median filtering, covering all stages from DICOM acquisition to STL-based 3D printing preparation

During the median filtering phase, four kernel sizes, 3×3, 5×5, 7×7, and 9×9, were utilized with MATLAB's medfilt2 function. No quantitative metrics such as PSNR or SSIM were applied in this stage; however, the filtered outputs were qualitatively compared for noise suppression, anatomical

border clarity, and visual print quality. The 3×3 kernel exhibited the most advantageous compromise. The filtered images preserved anatomical border clarity and removed high-frequency noise, thereby offering a reliable foundation for further segmentation and modeling tasks.

After filtering, thresholding and segmentation were used to highlight anatomical features such as bones and soft tissues based on specific HU ranges determined through experimentation (for example, >200 HU for bone). Binary masks were created to define pertinent anatomical areas, serving as the foundation for volume depiction.

A. Segmentation and Thresholding

The DCM_01.rar archive [78], which is accessible at [https://zenodo.org/records/15244881/files/DCM_01.rar?download=1], was accessed to obtain a publicly available CT chest dataset for preliminary preprocessing. MATLAB R2024b was employed to accomplish this task. This collection consists of 813 anonymized DICOM segments in a standard 16-bit grayscale format, each with a spatial resolution of 512×512 pixels. The data were acquired using a helical CT scan technique and have been completely de-identified in accordance with international privacy standards.

The DICOM series was imported into MATLAB for preprocessing. The Hounsfield Unit (HU) values of anatomical areas of interest, primarily osseous structures, were used to delineate them using intensity-based thresholding. Non-relevant regions, such as soft tissues and air, were excluded, and voxels exceeding 200 HU were identified as bone tissue. In the absence of metadata fields such as PixelSpacing and SliceThickness, all measurements and filtering evaluations were conducted at the pixel level without spatial calibration. To improve anatomical contrast, the HU thresholds were determined by clinical imaging standards and visual inspection.

The binary templates that were generated were employed for the purpose of volumetric reconstruction, segmentation, and additional denoising. No annotated ground-truth segmentation masks were available for benchmarking, so qualitative validation relied on visual consistency with anatomical references derived from standard CT atlases and prior literature. No clinical expert validation or inter-observer assessment was performed, which is acknowledged as a limitation and an area for future improvement. The 3D compilation of the original DICOM segments is illustrated in Fig. 2, which facilitates 3D rendering and multiplanar visualization (axial, sagittal, and coronal). These outputs are well-suited for research, instructional purposes, and preliminary prototyping in biomedical engineering applications.

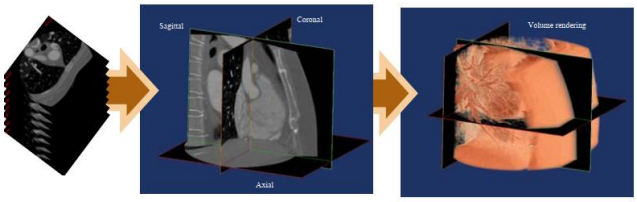

Fig. 2. Workflow of CT image processing, starting from stacked DICOM slices (left), through multiplanar reformatting (middle), to final 3D volume rendering (right)

B. Segmentation and Thresholding

The quality of medical imaging is significantly enhanced by noise reduction, particularly in CT scans that are used for 3D reconstruction and anatomical modeling. Salt-and-pepper noise is a notable occurrence, characterized by the arbitrary arrangement of brilliant and dark pixels. This noise has the potential to substantially alter anatomical boundaries and reduce the accuracy of segmentation, potentially affecting the reliability of downstream applications including surgical planning, diagnosis, and 3D printing.

Median filtering is the primary preprocessing technique employed in this investigation to address this matter. It is a nonlinear technique that is highly regarded for its ability to reduce impulse noise while preserving critical edge details. This method is especially advantageous in medical applications that necessitate precise organ boundary identification. Unlike linear filters such as the mean filter, which may blur structural features, the median filter replaces each pixel with the median value of its neighborhood, thereby supporting the retention of fine anatomical structures.

The primary objective of this investigation is to enhance the precision of CT image data obtained from a modified DICOM dataset by employing median filtering. To mitigate noise artifacts before key operations, the filtering process is performed prior to thresholding and 3D model generation.

This section outlines the justification for applying median filtering and presents the framework adopted to assess its effectiveness.

The subsequent sections explain (1) why different median filter window sizes were chosen and how they were selected based on visual fidelity and processing considerations and (2) the steps taken using MATLAB, including preparation steps and the method used to measure how well noise was reduced, how long processing took, and how well anatomical details were kept.

C. Choice of Median Filter

An often-occurring artifact in medical imaging, especially in CT scans, is salt-and-pepper noise. It appears as haphazardly distributed high-contrast pixels that significantly reduce image quality and compromise the accuracy of subsequent image segmentation and 3D reconstruction. Such noise introduces abrupt intensity variations that are challenging to remove using traditional linear filters. The median filter, a nonlinear spatial filter that is effective in reducing impulsive noise while preserving the structural integrity of anatomical details, is employed in this study to resolve this issue. The median filter replaces the intensity of each pixel with the median value of its neighbors, in contrast to linear filters like the Gaussian or average filter, which frequently blur boundaries. By refraining from averaging, which would otherwise obfuscate fine details, this replacement mechanism maintains sharp anatomical boundaries. This method is especially beneficial for the precise preservation of organ boundaries, which is crucial for clinical applications.

The median filtering process is quantitatively expressed by the following (1).

$$g(x,y) = median\{f(i,j)|(i,j) \in \omega(x,y)\} \quad (1)$$

where $f(i,j)$ represents the original intensity values inside the neighborhood $\omega(x,y)$, and $g(x,y)$ indicates the output intensity following filtering. This formulation effectively removes outlier values while preserving surrounding anatomical consistency.

Four different window sizes (3×3, 5×5, 7×7, and 9×9) were evaluated in this work. Each size offers a different balance between detail retention and noise-lowering effectiveness. Smaller windows retain more anatomical detail but may be less effective at eliminating extensive noise, whereas larger windows suppress noise more thoroughly but may reduce structural fidelity. The decision to assess several kernel sizes was motivated by the need to find the best trade-off between fidelity and efficiency.

As shown in Fig. 3, the 3×3 median filter ranks the intensity levels of every pixel within its local 3×3 neighborhood window (marked in red). In the example, the center pixel (highlighted in green) and its surrounding neighbors are used. The window's sorted pixel values allow one to choose a median value to replace the center pixel. Applying this method across the image results in a filtered output that maintains important structures and lowers impulse noise. The right panel in Fig. 3 shows clear edge preservation together with noise artifact reduction, thereby demonstrating the pragmatic efficiency of median filtering.

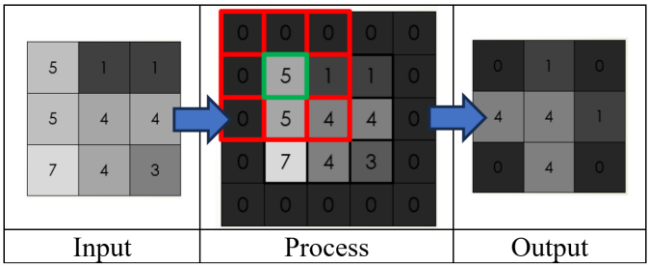

Fig. 3. Example of 3×3 median filtering

D. Implementation

This work used 813 axial CT images in DICOM format, each with a 16-bit grayscale depth and 512×512 pixels. Obtained from the CT chest collection "DCM_01," which was developed to comply with clinical imaging guidelines and is publicly accessible and anonymized, these images were used for analysis. For preprocessing, each segment was imported in MATLAB R2024b using the functions "dicominfo" and "dicomread". Bit-depth normalization and grayscale scaling were used to standardize intensity representation across all segments.

Using four different square kernel sizes (3×3, 5×5, 7×7, and 9×9), the aim was to reduce salt-and-pepper noise across all images. This was accomplished using the built-in function medfilt2. This filtering made comparative evaluation of anatomical detail retention against noise suppression possible. The syntax employed in this procedure is delineated in (2).

$$filteredImage = medfilt2(originalImage, [w\ w]) \quad (2)$$

The variable w denotes the width of the square kernel and belongs to the set $\{3,5,7,9\}$. Every image underwent filtering separately to ensure consistency and preserve localized control. Archived and then evaluated using FlashPrint 5 tools, the filtered sections served for visual inspection and 3D model building.

For each kernel size, key performance parameters were recorded, including approximate processing time per segment, edge fidelity, and visual noise reduction. These assessments helped to identify the 3×3 kernel arrangement that offers the best desired balance between anatomical integrity and filtering performance. Quantitative metrics were not computed, which is acknowledged as a limitation and will be addressed in future investigations.

E. Mean Filtering for Noise Reduction

The mean filter is a fundamental linear filtering technique that is frequently employed in the field of image processing to attenuate noise and normalize images. It operates by replacing each pixel with the average value of its neighboring pixels within a predetermined window size. This technique is effective in reducing Gaussian noise or minor intensity variations by smoothing random fluctuations in pixel intensity.

The mathematical expression of the mean filter's output at pixel location (x,y) is as follows (3).

$$g(x,y) = \frac{1}{N}\sum_{(i,j\in\omega(x,y))} f(i,j) \quad (3)$$

The intensity value of the input image at coordinates (i,j) is denoted by $f(i,j)$, while the neighborhood window centered around the pixel at (x,y) is defined by $\omega(x,y)$. The variable N represents the total number of pixels in the window, such as 9 for a 3×3 kernel. The average of all pixel values within the window is used to calculate the output intensity $g(x,y)$. This method smooths local intensity variations but may blur structural boundaries.

The computational simplicity and ease of implementation of the mean filter make it advantageous in general image processing tasks. Nevertheless, its primary drawback is its tendency to blur edges and reduce structural clarity. The uniform treatment of all pixels within the window frequently mitigates abrupt transitions, such as edges or complex anatomical structures, which are essential in medical imaging applications such as CT and MRI.

The mean filter is less suitable for tasks that require structural accuracy, such as organ segmentation or 3D model generation, due to its tendency to degrade anatomical boundaries, even though it improves image uniformity in medical applications. In such contexts, median filtering is the preferable method because it effectively eliminates impulsive noise, including salt-and-pepper noise, while preserving edges.

In conclusion, the mean filter is appropriate for general-purpose denoising, but its application in high-precision medical imaging requires careful evaluation, especially when the preservation of anatomical detail is critical.

F. Model Refinement, 3D Reconstruction, and Printing Workflow

The erase tool in FlashPrint 5 was utilized to manually eradicate any remaining noise artifacts, such as floating

voxels, speckle noise, or broken parts, following the median filtering and segmentation procedure. This step helped improve model clarity and reduce non-anatomical fragments, enhancing the suitability of the model for fabrication using FDM printing. The erase function effectively eliminated false-positive areas that were introduced by thresholding or aggressive filtration while preserving the main anatomical features.

Subsequently, a comprehensive 3D organ model was produced by volumetrically stacking the filtered and corrected image slices. The model was converted into a surface geometry using MATLAB and FlashPrint 5, and the resulting file was exported in STL format for slicing applications. In order to prevent printing failures and maintain the structure of the model, the mesh structure of each STL file was visually examined, and obvious artifacts were manually removed.

The desktop FDM 3D printer was utilized, and FlashPrint 5 was the slicing software employed in the construction stage. PLA filament was used for printing, and its specifications included a layer height of 0.1 to 0.2 mm, an infill density of 15 percent to 25 percent, and a nozzle temperature of 210 degrees Celsius. These printing parameters were selected to achieve stable fabrication and recognizable anatomical form.

The computational framework for image processing and reconstruction efficiently processed the 813-slice dataset on a workstation outfitted with an Intel Core i7 CPU, 32 GB of RAM, and 1 TB of SSD storage, utilizing MATLAB R2024b. A consistent pipeline was implemented for converting CT data affected by noise into 3D-printable anatomical representations through filtering, manual refinement, model reconstruction, and physical printing.

The STL file generated by MATLAB and prepared in FlashPrint 5 prior to 3D printing is illustrated in Fig. 4. The reconstructed rib and pelvic skeleton model from CT data is depicted in the left panel, while the same model with automatically generated support structures is depicted in the right panel. This example demonstrates the connection between digital processing and fabrication steps in anatomical modeling workflows.

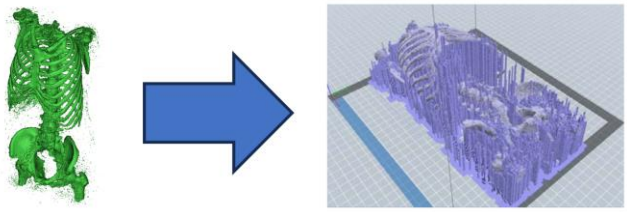

Fig. 4. STL file of the rib and pelvic skeleton created in MATLAB and configured in FlashPrint 5 with automatically built supports for 3D printing

III. Results and Discussion

The median filter's efficacy in noise reduction and its influence on the reconstruction of 3D models were assessed using a CT dataset featuring 813 DICOM segments (512×512 pixels, 16-bit grayscale). The study evaluated the efficacy of four distinct median filter window sizes, 3×3, 5×5, 7×7, and 9×9, in suppressing salt-and-pepper noise while maintaining anatomical fidelity. The evaluation was conducted through visual inspection rather than quantitative image quality metrics due to the lack of ground truth annotations and the unavailability of standardized segmentation references. The primary emphasis was placed on visual clarity and practical feasibility for medical 3D printing rather than statistical image analysis, which is acknowledged as a methodological limitation in this experimental study.

A. Comparative Examination of Filtering Methods for CT Spine Visualization

The initial part of the image processing technique involved selecting an area of interest (ROI) from a standard axial CT slice. This step was intended to evaluate the preliminary effectiveness of the pipeline in separating anatomical features before the application of further segmentation and 3D reconstruction techniques.

Fig. 5(a) shows the raw CT slice, highlighting different body parts such as bone, soft tissue, and air spaces, along with a basic grayscale intensity pattern. A basic thresholding method was applied to identify clinically significant regions. The threshold range was manually adjusted through visual inspection until skeletal structures, including ribs and spinal segments, were sufficiently separated. Fig. 5(b) shows the initial selection, with green highlights indicating the areas identified based on this visual segmentation.

The segmentation results were improved through filtering and noise reduction after thresholding, as illustrated in Fig. 5(c). This resulted in a more precise and focused representation. Soft tissue artifacts and background noise were minimal, while key features and skeletal structures persisted. This refinement step contributed to improved visual clarity and supported STL export for subsequent 3D printing.

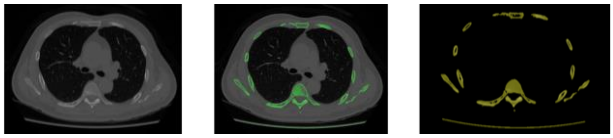

(a) (b) (c)

Fig. 5. CT image preprocessing workflow: (a) original, (b) segmented ROI, (c) final binary mask

The simplicity and adaptability of this threshold-based method are its greatest assets. Specific threshold values were not predefined; however, dynamic adjustments were implemented for each scan to improve visibility and anatomical precision. The results indicate that when combined with visual confirmation and domain knowledge, fundamental segmentation techniques can yield dependable results.

In general, this segmentation procedure is a critical preprocessing stage that converts raw CT data into refined binary masks. It guarantees that the final model contains only pertinent anatomical structures and reinforces the stability of downstream tasks in MATLAB and 3D reconstruction workflows.

B. Comparative Examination of Filtering Methods for CT Spine Visualization

This study assessed the effectiveness of several filtering techniques in enhancing CT image quality for 3D reconstruction through visual and comparative evaluations of multiple image preprocessing methods. The focus was on

preserving anatomical integrity, particularly the spinal structure, while effectively reducing salt-and-pepper noise.

Fig. 6 shows sagittal CT scans of the spine that have been processed through several stages. The original image Fig. 6(A) contained a considerable amount of high-contrast noise, but raw anatomical features were retained. A thresholding process was used in Fig. 6(B) to separate skeletal components and eliminate soft tissue. In order to improve the contrast between bone features and background and enable more accurate segmentation, the threshold range was manually adjusted through visual inspection.

A 3×3 mean filter was used in Fig. 6(C), which produced a smoother output but blurred small bony structures and reduced edge definition. On the other hand, the 3×3 median filter in (D) significantly reduced high-frequency noise while preserving edge sharpness. As the kernel size was increased to 5×5, 7×7, and 9×9 Fig. 6(E) to (G), over-smoothing caused an increasing loss of anatomical detail.

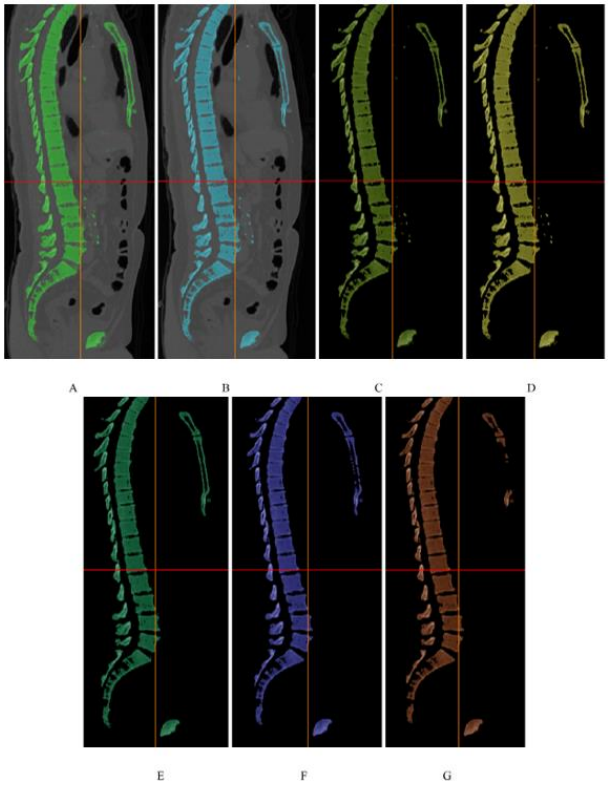

Fig. 6. Sample 2D CT image processing: (A) original, (B) thresholded (130-1500), (C) mean 3×3, (D) median 3×3, (E) median 5×5, (F) median 7×7, (G) median 9×9

These differences are more noticeable in Fig. 7, which shows a magnified view of the lumbar spine region. While larger window sizes Fig. 7(F) and (G) made it harder to see vertebral boundaries, the 3×3 median filter reduced noise while maintaining structural clarity. The mean filter Fig. 7(C) resulted in transition blurring and disrupted the continuity between adjacent vertebrae.

The comparative outcomes of the filtering techniques are summarized in Table I. The best visual quality was shown by the 3×3 median filter, which successfully reduced noise while preserving anatomical features. Stronger noise reduction was achieved with larger kernel sizes, but fine skeletal features were significantly lost, especially in areas with faint edge transitions.

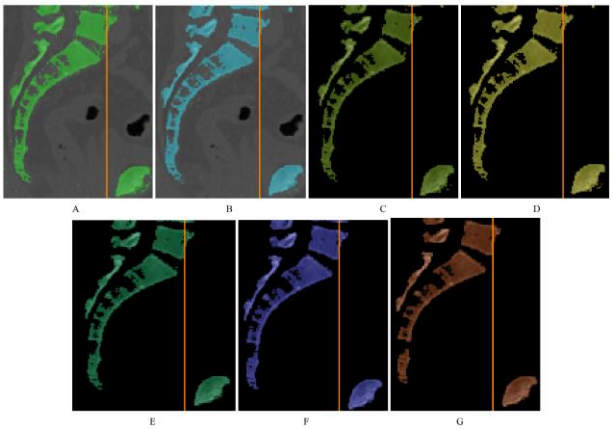

Fig. 7. Close-up view of CT slice filtering results: (A) original, (B) thresholded (130-1500), (C) mean 3×3, (D) median 3×3, (E) median 5×5, (F) median 7×7, (G) median 9×9

TABLE I. QUALITATIVE COMPARISON OF FILTERING PERFORMANCE ON CT IMAGES

Filter Type	Noise Removal	Edge Clarity	Anatomical Detail	Visual Quality
Mean 3×3	Moderate	Low	Blurred	Fair
Median 3×3	High	High	Preserved	Excellent
Median 5×5	Very High	Moderate	Slightly blurred	Good
Median 7×7	Very High	Low	Flattened	Fair
Median 9×9	Very High	Very Low	Flattened	Poor

Due to the absence of annotated ground truth, the evaluation was based on qualitative visual inspection rather than statistical validation. Metrics such as PSNR, SSIM, or edge preservation scores were not applied. The emphasis was on practical outcomes relevant to 3D printing and segmentation workflows, despite the limitations in numerical benchmarking.

These results are in line with earlier studies that show median filters preserve important edge information in medical imaging better than mean filters, especially for bone structures. This work is unique in that it confirms that the 3×3 kernel offers a good trade-off between fidelity and filtering efficiency by applying these observations to a real-world 3D printing scenario.

The findings support that the 3×3 median filter is the most suitable option for preprocessing CT data for anatomical modeling. It minimizes the need for further correction while supporting diagnostic precision, especially when threshold values are carefully adjusted for each dataset. Larger filters may be acceptable in low-detail applications but are not recommended for tasks involving skeletal segmentation.

C. Evaluation and Comparison of Median Filter Effectiveness

The performance of median filters applied to CT images derived from DICOM data with varying kernel sizes was investigated in this study. These images enabled the

construction of precise three-dimensional medical models, where anatomical fidelity is crucial.

Applying each median filter size to the initial CT slices was the first step in the evaluation. To evaluate the degree of noise reduction and anatomical contour preservation, the results were visually examined. As demonstrated in Fig. 8, the 3×3 median filter successfully removed small noise while preserving anatomical structure and edge sharpness. Significant smoothing was introduced by larger filters, like 7×7 and 9×9 (see Fig. 8(E)), which reduced boundary clarity and eliminated fine anatomical information. To examine filter performance in localized regions, Fig. 9 presents an enlarged pixel cluster containing 64 pixels. In this context, the 3×3 median filter demonstrated good noise reduction while maintaining pixel structure, especially in regions with delicate intensity changes or complex textures.

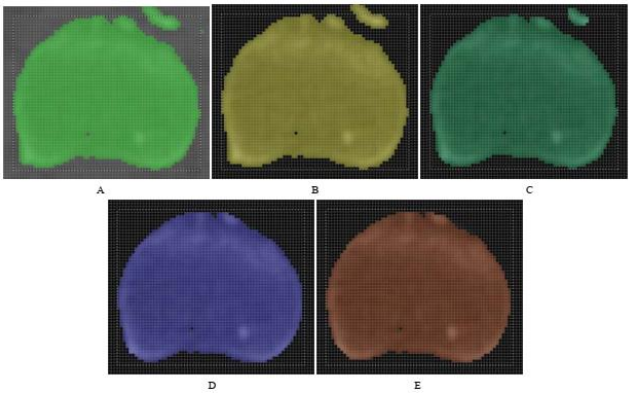

Fig. 8. Median filtering results for a CT region with size 66 × 55 pixels. (A) Original image, (B) Median filter 3×3, (C) Median filter 5×5, (D) Median filter 7×7, (E) Median filter 9×9

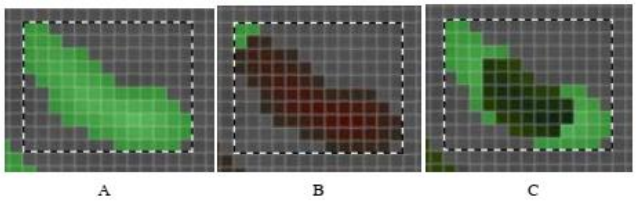

Fig. 9. Example of a small pixel cluster consisting of 64 pixels. (A) Original image, (B) Median filter 3×3, (C) Median filter 5×5

A comparison with the mean filter was conducted to highlight the relative advantages of median filtering. As shown in Fig. 10, four images are displayed in sequence: the original, the thresholded version, and the outputs from the mean and median filters. Compared to the mean filter, the 3×3 median filter showed superior edge retention and noise reduction. More intricate anatomical shapes were the subject of additional comparisons. For example, a region with irregular contours and curvature is shown in Fig. 11. While the mean filter blurred internal boundaries, the 3×3 median filter produced more distinct structural edges. The observed benefit of median filtering is further supported by Fig. 12 and Fig. 13, which show this behavior in smaller segmented regions with various geometric properties.

The collective visual evidence from Fig. 8 to Fig. 13 indicates that the 3×3 median filter is the most effective in reducing noise while preserving anatomical accuracy. Larger window sizes, on the other hand, frequently resulted in over-smoothing and the loss of clinically meaningful detail.

Since there were no annotated ground truth data available for quantitative comparison, this evaluation was done solely visually. One known drawback is that no statistical measures like SSIM or Dice scores were calculated. Instead of objectively benchmarking image quality, the focus was on the usefulness of filtered images for 3D reconstruction and printing.

These outcomes are consistent with prior research findings, which reported that median filtering is more effective than linear filters in preserving edge features in medical imaging, especially for osseous structures. While those prior studies emphasized algorithmic evaluation, this work applies such findings to a physical 3D modeling workflow and demonstrates that the 3×3 kernel offers a practical and efficient balance between detail preservation and noise suppression.

The results support the conclusion that the 3×3 median filter is the most appropriate choice for CT preprocessing in anatomical modeling. Particularly when threshold values are customized for specific datasets, it minimizes the need for post-processing while maintaining diagnostic integrity. Larger filters are generally discouraged for tasks involving bone segmentation, though they might be useful in situations where high detail is not required.

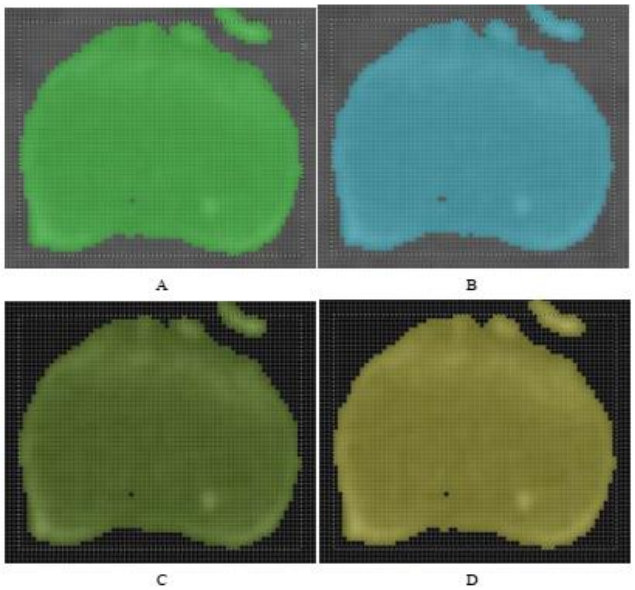

Fig. 10. Comparison of image filtering results for a region with size 66 × 55 pixels. (A) Original image, (B) Thresholded image, (C) Mean filter 3×3, (D) Median filter 3×3

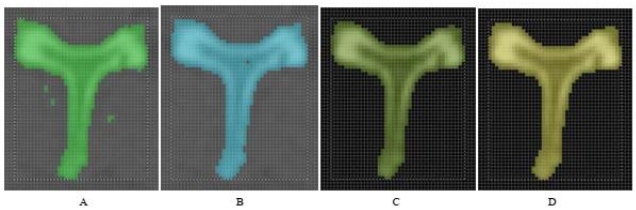

Fig. 11. Comparison of image filtering results for a complex region with size 40 × 48 pixels. (A) Original image, (B) Thresholded image (130-1500), (C) Mean filter 3×3, (D) Median filter 3×3

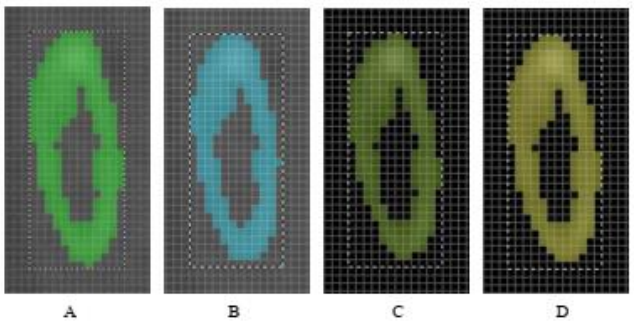

Fig. 12. Example of segmented region with size 12 × 30 pixels. (A) Original image, (B) Thresholded image (130-1500), (C) Mean filter 3×3, (D) Median filter 3×3

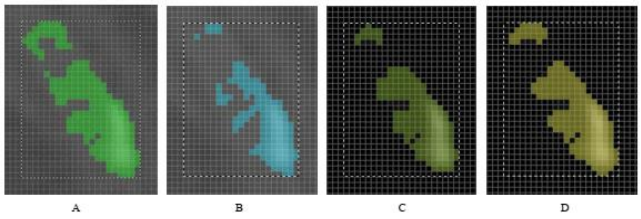

Fig. 13. Example of segmented region with size 21 × 28 pixels. (A) Original image, (B) Thresholded image (130-1500), (C) Mean filter 3×3, (D) Median filter 3×3.

D. Assessment of 3D Model Precision Post Noise Mitigation

This section assesses the influence of median filtering on the precision of 3D reconstructions obtained from DICOM-formatted CT scan data. Four preprocessing strategies were analyzed, including original pictures, thresholding without filtering, a 3×3 mean filter, and a 3×3 median filter. The reconstructed models were examined in three dimensions to assess structural clarity and residual noise artifacts.

Fig. 14 demonstrates that thresholding alone produced considerable surface abnormalities, notably fine voxel clusters linked to salt-and-pepper noise. The mean filter, although generating smoother surfaces, induced blurring effects that obscured fine anatomical contours such as spinal outlines and rib curvatures, thereby reducing visibility. In contrast, the application of the 3×3 median filter preserved skeletal boundaries while effectively minimizing random noise, resulting in structurally coherent models.

These conclusions are further substantiated by the broadened viewpoint in Fig. 15. The raw and thresholded datasets clearly displayed irregularities and discontinuities, whereas the median-filtered reconstruction exhibited smoother and more continuous anatomical outlines. The mean filter compromised the visual clarity of critical skeletal features, which may affect diagnostic interpretability.

The results collectively offer persuasive qualitative evidence that the 3×3 median filter effectively balances noise reduction with the preservation of anatomical detail. This observation aligns with earlier research highlighting the strength of median filtering in edge preservation, especially in bone-focused imaging contexts. Although no quantitative metrics were calculated, the visual consistency and structural integrity of the output validate the practical use of the 3×3 median filter in clinical modeling and medical prototyping.

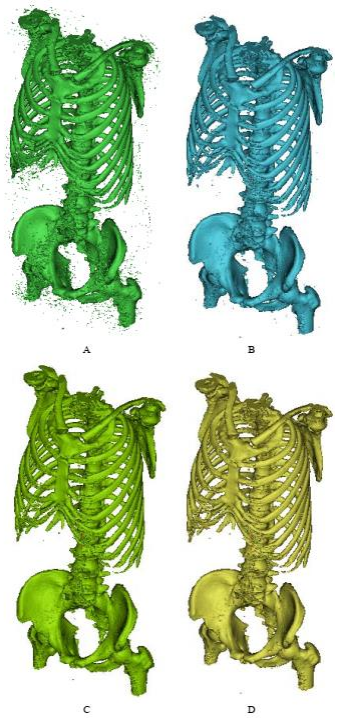

Fig. 14. 3D Bone Model Comparison Using Different Filtering Techniques: (A) Original Image, (B) Thresholding (130-1500), (C) Mean Filter 3×3, (D) Median Filter 3×3

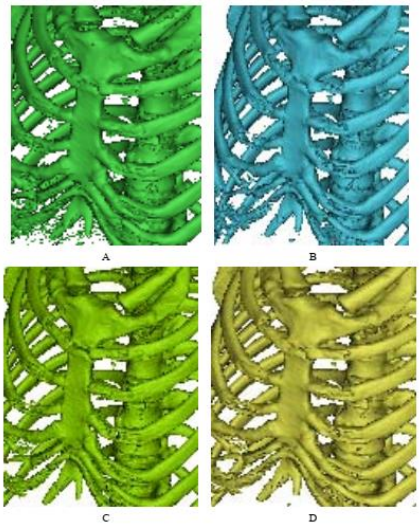

Fig. 15. Zoomed-in Rib Cage Region Comparison: (A) Original Image, (B) Thresholding (130-1500), (C) Mean Filter 3×3, (D) Median Filter 3×3

E. Assessment of 3D Model Readiness through Slicing Simulation and Material Estimation

This investigation assessed the preparedness of CT-derived anatomical models for 3D printing with FlashPrint software. The workflow encompassed slicing simulation, support generation, and material consumption estimation. Three preprocessing procedures were evaluated, including thresholding without filtering, the use of a 3×3 average filter followed by thresholding, and the use of a 3×3 median filter followed by thresholding.

The results illustrated in Fig. 16 through Fig. 18 and Table II indicate that thresholding alone produced the maximum number of support structures and the largest filament usage,

amounting to 103.67 meters. The total print duration was almost 61 hours and 3 minutes. The pronounced voxel-level noise seen in the unfiltered model led to suboptimal material use and extended fabrication time.

The application of an average filter prior to thresholding significantly diminished noise artifacts, which consequently enhanced the surface smoothness of the resultant model. This method, however, also resulted in edge blurring, reducing anatomical clarity. Filament usage was minimized to 90.26 meters, and the printing time was shortened to 40 hours and 25 minutes.

The utilization of a 3×3 median filter yielded the most structurally distinct and print-optimized model. This arrangement maintained essential anatomical contours while reducing superfluous supports. Consequently, filament consumption was diminished to 85.13 meters, with the projected printing duration being 50 hours and 1 minute. As shown in Table II, the model processed with a 3×3 median filter necessitated the least filament and produced the most balanced print duration. This configuration resulted in an 18.07 percent reduction in time and a 17.88 percent drop in material usage compared to the unfiltered baseline. These findings underscore the practical advantage of incorporating median filtering into the preprocessing pipeline for medical 3D printing.

The results confirm that a 3×3 median filter improves printing efficiency while better maintaining anatomical characteristics compared to average filtering or unfiltered thresholding. This method corresponds with the overarching goal of enhancing computational models for subsequent physical reconstruction in biomedical applications.

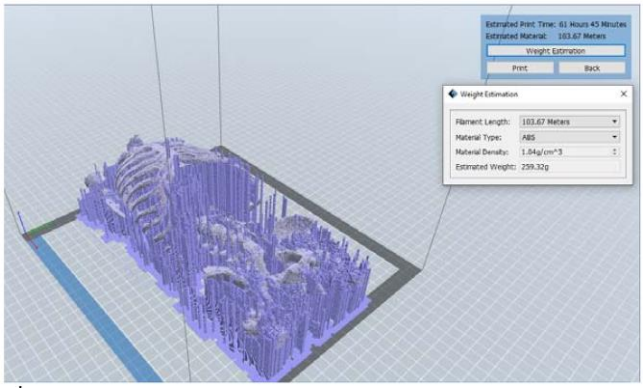

Fig. 16. 3D model Preview from thresholded CT data without filtering

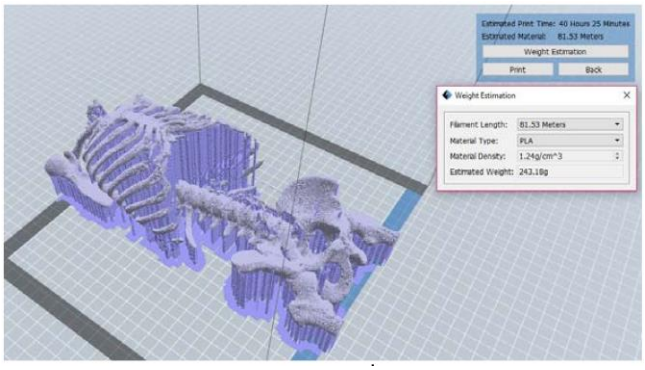

Fig. 17. 3D model preview with average filter 3×3 and thresholding

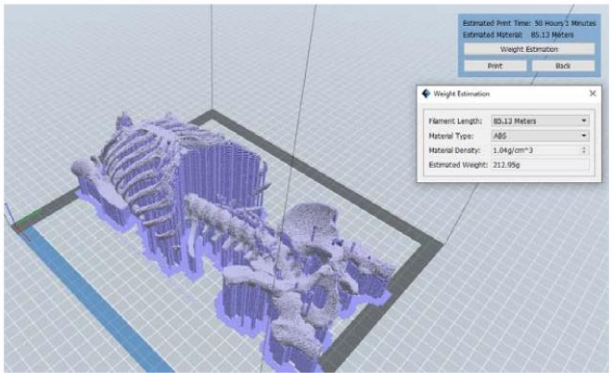

Fig. 18. 3D model preview with median filter 3×3 and thresholding

TABLE II. COMPARISON OF 3D PRINTING TIME AND FILAMENT CONSUMPTION BASED ON PREPROCESSING METHODS

Method	Thresholding Only	Avg Filter 3×3 + Thresholding	Median Filter 3×3 + Thresholding
Print Time	61h 3min	40h 25min	50h 1min
Filament Used (m)	103.67	90.26	85.13
Time Saved (min)	-	1248	661
Time Saved (%)	-	34.05%	18.07%
Filament Saved (m)	-	13.41	18.54
Filament Saved (%)	-	12.94%	17.88%

IV. CONCLUSION

This study presents an effective technique to improve the accuracy of 3D organ models obtained from CT medical images by utilizing a 3×3 median filter alongside further manual modification. The suggested method efficiently diminishes salt-and-pepper noise while maintaining anatomical features crucial for precise 3D reconstructions. The 3×3 median filter attained the most equitable compromise between noise reduction and structural integrity, enhancing the surface quality of models while maximizing material efficiency for 3D printing. These advantages indicate the method's potential utility in medical environments, such as anatomical modeling for clinical teaching. However, the current study does not include clinical validation or cross-dataset performance, so its broader applicability remains uncertain. Nonetheless, additional confirmation is required prior to incorporation into diagnostic or surgical planning protocols. The limitations of this study include the lack of quantitative image quality assessments, such as the Dice coefficient or SSIM, and reliance on a single dataset that lacks anatomical variety. The segmentation pipeline depends on manually adjusted thresholds and deletion steps, which may affect repeatability and scalability. Furthermore, no physical measurement or expert-based validation of printed outputs was conducted to confirm anatomical accuracy. Future research may address these constraints by incorporating automated, AI-driven segmentation methods, such as U-Net or GANs, to improve accuracy and applicability. Extending experiments to heterogeneous datasets and incorporating reproducibility controls is also essential. Investigating comparative benchmarking alongside advanced denoising methods and the physical validation of printed models is crucial to enhance therapeutic significance.

ACKNOWLEDGMENT

The researcher would like to thank the Research Institute, Academic Services Center, and College of Biomedical Engineering, Rangsit University for the grant of research funding to the research team. The authors would like to convey their profound appreciation to Assoc. Prof. Dr. Manas Sangworasil and Prof. Dr. Takenobu Matsuura for their foundational advice and oversight during the first phases of this research effort. Their mentorship offered essential guidance for the effective completion of the project. Furthermore, it is confirmed that the project has been reviewed by the Ethics Review Board of Rangsit University, with reference number RSUERB2025-007, which certifies that the research does not involve human subjects. Moreover, AI-driven methods (QuillBot Premium) were utilized for grammatical verification, paraphrasing, and linguistic augmentation to ensure the accuracy and clarity of the text. All CT DICOM images included in this investigation were anonymized prior to analysis. The anonymization process involved removing any personal health information (PHI) and anything related to the patient's identity, hospital, study details, device serial numbers, and private DICOM tags. The experiment was conducted in accordance with established rules for ethical data exchange and the protection of human subjects.

REFERENCES

[1] R. T. Sadia, J. Chen, and J. Zhang, "CT image denoising methods for image quality improvement and radiation dose reduction," *Journal of Applied Clinical Medical Physics*, vol. 25, no. 2, p. e14270, 2024, doi: 10.1002/acm2.14270.

[2] F. Fan *et al*., "Quadratic autoencoder (Q-AE) for low-dose CT denoising," *IEEE Transactions on Medical Imaging*, vol. 39, no. 6, pp. 2035-2050, 2019, doi: 10.1109/TMI.2019.2963248.

[3] R. Muwardi, M. Yunita, H. Ghifarsyam, and H. Juliyanto, "Optimize Image Processing Algorithm on ARM Cortex-A72 and A53," *Jurnal Ilmiah Teknik Elektro Komputer Dan Informatika*, vol. 8, no. 3, pp. 399-409, 2022, doi: 10.26555/jiteki.v8i3.24457.

[4] D. Sharma and N. Agrawal, "Development of Modified CNN Algorithm for Agriculture Product: A Research Review," *Jurnal Ilmiah Teknik Elektro Komputer Dan Informatika*, vol. 8, no. 1, pp. 167-174, 2022, doi: 10.26555/jiteki.v8i1.23722.

[5] R. Bello and C. Oluigbo, "Deep Learning-Based SOLO Architecture for Re-Identification of Single Persons by Locations," *Jurnal Ilmiah Teknik Elektro Komputer Dan Informatika*, vol. 8, no. 4, pp. 599-609, 2022, doi: 10.26555/jiteki.v8i4.25059.

[6] B. Suprapto, A. Wahyudin, H. Hikmarika, and S. Dwijayanti, "The Detection System of Helipad for Unmanned Aerial Vehicle Landing Using YOLO Algorithm," *Jurnal Ilmiah Teknik Elektro Komputer Dan Informatika*, vol. 7, no. 2, pp. 193-206, 2021, doi: 10.26555/jiteki.v7i2.20684.

[7] R. Bello, C. Oluigbo, and O. Moradeyo, "Motorcycling-Net: A Segmentation Approach for Detecting Motorcycling Near Misses," *Jurnal Ilmiah Teknik Elektro Komputer Dan Informatika*, vol. 9, no. 1, pp. 96-106, 2023, doi: 10.26555/jiteki.v9i1.25614.

[8] A. Kamilaris and F. X. Prenafeta-Boldú, "A review of the use of convolutional neural networks in agriculture," *The Journal of Agricultural Science*, vol. 156, no. 3, pp. 312-322, Mar. 2018, doi: 10.1017/S0021859618000436.

[9] R. H. Abiyev and M. K. S. Ma'aitaH, "Deep convolutional neural networks for chest diseases detection," *Journal of Healthcare Engineering*, vol. 2018, pp. 1-16, Nov. 2018, doi: 10.1155/2018/4168538.

[10] F. Schwendicke, T. Golla, M. Dreher, and J. Krois, "Convolutional neural networks for dental image diagnostics: A scoping review," *Journal of Dentistry*, vol. 91, p. 103226, Mar. 2019, doi: 10.1016/j.jdent.2019.103226.

[11] G. N. Nguyen, N. H. Le Viet, M. Elhoseny, K. Shankar, B. B. Gupta, and A. A. Abd El-Latif, "Secure blockchain enabled Cyber-physical systems in healthcare using deep belief network with ResNet model," *Journal of parallel and distributed computing*, vol. 153, pp. 150-160, 2021, doi: 10.1016/j.jpdc.2021.03.011.

[12] C. D. Vo, D. A. Dang, and P. H. Le, "Development of Multi-Robotic Arm System for Sorting System Using Computer Vision," *Journal of Robotics and Control (JRC)*, vol. 3, no. 5, pp. 690-698, 2022, doi: 10.18196/jrc.v3i5.15661.

[13] A. N. Hidayah, S. A. Radzi, N. A. Razak, W. H. M. Saad, Y. C. Wong, and A. A. Naja, "Disease Detection of Solanaceous Crops Using Deep Learning for Robot Vision," *Journal of Robotics and Control (JRC)*, vol. 3, no. 6, pp. 790-799, 2022, doi: 10.18196/jrc.v3i6.15948.

[14] Z. Zou, K. Chen, Z. Shi, Y. Guo, and J. Ye, "Object Detection in 20 Years: A Survey," in *Proceedings of the IEEE*, vol. 111, no. 3, pp. 257-276, March 2023, doi: 10.1109/JPROC.2023.3238524.

[15] P. Rosyady and R. Sumiharto, "Highway Visual Tracking System using Thresholding and Hough Transform," *Jurnal Ilmiah Teknik Elektro Komputer Dan Informatika*, vol. 4, no. 2, pp. 93-99, 2019, doi: 10.26555/jiteki.v4i2.12016.

[16] T. Agrawal and P. Choudhary, "Segmentation and classification on chest radiography: a systematic survey," *The Visual Computer*, vol. 39, no. 3, pp. 875-913, 2023, doi: 10.1007/s00371-021-02352-7.

[17] S. Saha Roy, S. Roy, P. Mukherjee, and A. Halder Roy, "An automated liver tumour segmentation and classification model by deep learning based approaches," *Computer Methods in Biomechanics and Biomedical Engineering: Imaging & Visualization*, vol. 11, no. 3, pp. 638-650, 2023, doi: 10.1080/21681163.2022.2099300.

[18] M. Xu, K. Huang, and X. Qi, "A Regional-Attentive Multi-Task Learning Framework for Breast Ultrasound Image Segmentation and Classification," *IEEE Access*, vol. 11, pp. 5377-5392, 2023, doi: 10.1109/ACCESS.2023.3236693.

[19] A. Iqbal and M. Sharif, "BTS-ST: Swin transformer network for segmentation and classification of multimodality breast cancer images," *Knowledge-Based Systems*, vol. 267, p. 110393, 2023, doi: 10.1016/j.knosys.2023.110393.

[20] M. K. Hasan, M. A. Ahamad, C. H. Yap, and G. Yang, "A survey, review, and future trends of skin lesion segmentation and classification," *Computers in Biology and Medicine*, p. 106624, 2023, doi: 10.1016/j.compbiomed.2023.106624.

[21] T. Dang and H. Tran, "A Secured, Multilevel Face Recognition based on Head Pose Estimation, MTCNN and FaceNet," *Journal of Robotics and Control (JRC)*, vol. 4, no. 4, pp. 431-437, 2023, doi: 10.18196/jrc.v4i4.18780.

[22] M. I. Rusydi, A. Novira, T. Nakagome, J. Muguro, R. Nakajima, W. Njeri, et al., "Autonomous Movement Control of Coaxial Mobile Robot based on Aspect Ratio of Human Face for Public Relation Activity Using Stereo Thermal Camera," *Journal of Robotics and Control (JRC)*, vol. 3, no. 3, pp. 361-373, 2022, doi: 10.18196/jrc.v3i3.14750.

[23] X. Zheng, Q. Lei, R. Yao, Y. Gong, and Q. Yin, "Image segmentation based on adaptive K-means algorithm," *EURASIP Journal on Image and Video Processing*, vol. 2018, no. 1, pp. 1-10, 2018, doi: 10.1186/s13640-018-0309-3.

[24] R. Srikanth and K. Bikshalu, "Multilevel thresholding image segmentation based on energy curve with harmony Search Algorithm," *Ain Shams Engineering Journal*, vol. 12, no. 1, pp. 1-20, 2021, doi: 10.1016/j.asej.2020.09.003.

[25] G. Aletti, A. Benfenati, and G. Naldi, "A semiautomatic multi-label color image segmentation coupling Dirichlet problem and colour distances," *Journal of Imaging*, vol. 7, no. 10, p. 208, 2021, doi: 10.3390/jimaging7100208.

[26] C. Suguna and S. P. Balamurugan, "Computer Aided Diagnosis for Cervical Cancer Screening using Monarch Butterfly Optimization with Deep Learning Model," *in 2023 5th International Conference on Smart Systems and Inventive Technology (ICSSIT)*, pp. 1059-1064, 2023, doi: 10.1109/ICSSIT55814.2023.10060959.

[27] G. Sun, X. Jia, and T. Geng, "Plant diseases recognition based on image processing technology," *Journal of Electrical and Computer Engineering*, vol. 2018, 2018, doi: 10.1155/2018/6070129.

[28] A. Mohan and S. Poobal, "Crack detection using image processing: A critical review and analysis," *Alexandria Engineering Journal*, vol. 57, no. 2, pp. 787-798, 2018, doi: 10.1016/j.aej.2017.01.020.

[29] B. Li and Y. He, "An improved ResNet based on the adjustable shortcut connections," *IEEE Access*, vol. 6, pp. 18967-18974, 2018, doi: 10.1109/ACCESS.2018.2814605.

[30] D. Marmanis, K. Schindler, J. D. Wegner, S. Galliani, M. Datcu, and U. Stilla, "Classification with an edge: Improving semantic image segmentation with boundary detection," *ISPRS Journal of Photogrammetry and Remote Sensing*, vol. 135, pp. 158-172, 2018, doi: 10.48550/arXiv.1612.01337.

[31] J. Duan, T. Shi, H. Zhou, J. Xuan, and S. Wang, "A novel ResNet-based model structure and its applications in machine health monitoring," *Journal of Vibration and Control*, vol. 27, no. 9-10, pp. 1036-1050, 2021, doi: 10.1177/107754632093650.

[32] H. Yu, H. Sun, J. Tao, C. Qin, D. Xiao, Y. Jin, and C. Liu, "A multi-stage data augmentation and AD-ResNet-based method for EPB utilization factor prediction," *Automation in Construction*, vol. 147, p. 104734, 2023, doi: 10.1016/j.autcon.2022.104734.

[33] S. Ayyachamy, V. Alex, M. Khened, and G. Krishnamurthi, "Medical image retrieval using Resnet-18," *Medical Imaging 2019: Imaging Informatics for Healthcare, Research, and Applications*, vol. 10954, pp. 233-241, 2019, doi: 10.1117/12.2515588.

[34] M. Gao, D. Qi, H. Mu, and J. Chen, "A transfer residual neural network based on ResNet-34 for detection of wood knot defects," *Forests*, vol. 12, no. 2, p. 212, 2021, doi: 10.3390/f12020212.

[35] L. Wen, X. Li, and L. Gao, "A transfer convolutional neural network for fault diagnosis based on ResNet-50," *Neural Computing and Applications*, vol. 32, pp. 6111-6124, 2020, doi: 10.1007/s00521-019-04097-w.

[36] B. Yu, L. Yang, and F. Chen, "Semantic segmentation for high spatial resolution remote sensing images based on convolution neural network and pyramid pooling module," *IEEE Journal of Selected Topics in Applied Earth Observations and Remote Sensing*, vol. 11, no. 9, pp. 3252-3261, Sep. 2018, doi: 10.1109/JSTARS.2018.2860989.

[37] F. Tabassum, M. I. Islam, R. T. Khan, and M. R. Amin, "Human face recognition with combination of DWT and machine learning," *Journal of King Saud University-Computer and Information Sciences*, vol. 34, no. 3, pp. 546-556, 2022, doi: 10.1016/j.jksuci.2020.02.002.

[38] M. Sajjad, M. Nasir, K. Muhammad, S. Khan, Z. Jan, A. K. Sangaiah, et al., "Raspberry Pi assisted face recognition framework for enhanced law-enforcement services in smart cities," *Future Generation Computer Systems*, vol. 108, pp. 995-1007, 2020, doi: 10.1016/j.future.2017.11.013.

[39] L. Li, X. Mu, S. Li, and H. Peng, "A review of face recognition technology," *IEEE Access*, vol. 8, pp. 139110-139120, 2020, doi: 10.1109/ACCESS.2020.3011028.

[40] H. Ling, J. Wu, L. Wu, J. Huang, J. Chen, and P. Li, "Self residual attention network for deep face recognition," *IEEE Access*, vol. 7, pp. 55159-55168, 2019, doi: 10.1109/ACCESS.2019.2913205.

[41] A. Jha, "Classroom attendance system using facial recognition system," *The International Journal of Mathematics, Science, Technology, and Management*, vol. 2, no. 3, pp. 4-7, 2007, doi: 10.1051/itmconf/20203202001.

[42] R. I. Bendjillali, M. Beladgham, K. Merit, and A. Taleb-Ahmed, "Illumination-robust face recognition based on deep convolutional neural networks architectures," *Indonesian Journal of Electrical Engineering and Computer Science*, vol. 18, no. 2, pp. 1015-1027, 2020, doi: 10.11591/ijeecs.v18.i2.pp1015-1027.

[43] M. Z. Khan, S. Harous, S. U. Hassan, M. U. G. Khan, R. Iqbal, and S. Mumtaz, "Deep unified model for face recognition based on convolution neural network and edge computing," *IEEE Access*, vol. 7, pp. 72622-72633, 2019, doi: 10.1109/ACCESS.2019.2918275.

[44] A. Alzu'bi, F. Albalas, T. Al-Hadhrami, L. B. Younis, and A. Bashayreh, "Masked face recognition using deep learning: A review," *Electronics*, vol. 10, no. 21, p. 2666, 2021, doi: 10.3390/electronics10212666.

[45] Y. Tang, M. Chen, C. Wang, L. Luo, J. Li, G. Lian, and X. Zou, "Recognition and localization methods for vision-based fruit picking robots: A review," *Frontiers in Plant Science*, vol. 11, p. 510, 2020, doi: 10.3389/fpls.2020.00510.

[46] H. A. Williams, M. H. Jones, M. Nejati, M. J. Seabright, J. Bell, N. D. Penhall, *et al*., "Robotic kiwifruit harvesting using machine vision, convolutional neural networks, and robotic arms," *Biosystems Engineering*, vol. 181, pp. 140-156, 2019, doi: 10.1016/j.biosystemseng.2019.03.007.

[47] S. D. Kumar, S. Esakkirajan, S. Bama, and B. Keerthiveena, "A microcontroller based machine vision approach for tomato grading and sorting using SVM classifier," *Microprocessors and Microsystems*, vol. 76, p. 103090, 2020, doi: 10.1016/j.micpro.2020.103090.

[48] M. Halstead, C. McCool, S. Denman, T. Perez, and C. Fookes, "Fruit quantity and ripeness estimation using a robotic vision system," *IEEE Robotics and Automation Letters*, vol. 3, no. 4, pp. 2995-3002, 2018, doi: 10.1109/LRA.2018.2849514.

[49] S. Wan and S. Goudos, "Faster R-CNN for multi-class fruit detection using a robotic vision system," *Computer Networks*, vol. 168, p. 107036, 2020, doi: 10.1016/j.comnet.2019.107036.

[50] M. T. Habib, A. Majumder, A. Z. M. Jakaria, M. Akter, M. S. Uddin, and F. Ahmed, "Machine vision based papaya disease recognition," *Journal of King Saud University-Computer and Information Sciences*, vol. 32, no. 3, pp. 300-309, 2020, doi: 10.1016/j.jksuci.2018.06.006.

[51] J. J. Zhuang, S. M. Luo, C. J. Hou, Y. Tang, Y. He, and X. Y. Xue, "Detection of orchard citrus fruits using a monocular machine vision-based method for automatic fruit picking applications," *Computers and Electronics in Agriculture*, vol. 152, pp. 64-73, 2018, doi: 10.1016/j.compag.2018.07.004.

[52] A. Gongal, M. Karkee, and S. Amatya, "Apple fruit size estimation using a 3D machine vision system," *Information Processing in Agriculture*, vol. 5, no. 4, pp. 498-503, 2018, doi: 10.1016/j.inpa.2018.06.002.

[53] Z. Wang, J. Underwood, and K. B. Walsh, "Machine vision assessment of mango orchard flowering," *Computers and Electronics in Agriculture*, vol. 151, pp. 501-511, 2018, doi: 10.1016/j.compag.2018.06.040.

[54] X. Zhao, P. Sun, Z. Xu, H. Min, and H. Yu, "Fusion of 3D LIDAR and Camera Data for Object Detection in Autonomous Vehicle Applications," *IEEE Sensors Journal*, vol. 20, no. 9, pp. 4901-4913, 2020, doi: 10.1109/JSEN.2020.2966034.

[55] W. Zhao, W. Ma, L. Jiao, P. Chen, S. Yang, and B. Hou, "Multi-Scale Image Block-Level F-CNN for Remote Sensing Images Object Detection," *IEEE Access*, vol. 7, pp. 43607-43621, 2019, doi: 10.1109/ACCESS.2019.2908016.

[56] T. Zhou, D. P. Fan, M. M. Cheng, J. Shen, and L. Shao, "RGB-D Salient Object Detection: A Survey," *Computational Visual Media*, vol. 7, pp. 37-69, 2021, doi: 10.48550/arXiv.2008.00230.

[57] M. Shirpour, N. Khairdoost, M. Bauer, and S. Beauchemin, "Traffic Object Detection and Recognition Based on the Attentional Visual Field of Drivers," *IEEE Transactions on Intelligent Vehicles*, 2021, doi: 10.1109/TIV.2021.3133849.

[58] S. S. A. Zaidi, M. S. Ansari, A. Aslam, N. Kanwal, M. Asghar and B. Lee, "A Survey of Modern Deep Learning Based Object Detection Models," *Digital Signal Processing*, vol. 115, p. 103514, 2022, doi: 10.48550/arXiv.2104.11892.

[59] A. Kuznetsova *et al*., "The Open Images Dataset V4: Unified Image Classification, Object Detection, and Visual Relationship Detection at Scale," *International Journal of Computer Vision*, vol. 128, no. 7, pp. 1956-1981, 2020, doi: 10.48550/arXiv.1811.00982.

[60] X. Chen, H. Li, Q. Wu, K. N. Ngan, and L. Xu, "High-Quality R-CNN Object Detection Using Multi-Path Detection Calibration Network," *IEEE Transactions on Circuits and Systems for Video Technology*, vol. 31, no. 2, pp. 715-727, 2021, doi: 10.1109/TCSVT.2020.2987465.

[61] S. Zhang, Y. Wu, C. Men, and X. Li, "Tiny YOLO Optimization Oriented Bus Passenger Object Detection," *Chinese Journal of Electronics*, vol. 29, no. 1, pp. 132-138, 2020, doi: 10.1049/cje.2019.11.002.

[62] A. Suhail, M. Jayabalan, and V. Thiruchelvam, "Convolutional Neural Network Based Object Detection: A Review," *Journal of Critical Reviews*, vol. 7, no. 11, pp. 786-792, 2020, doi: 10.48550/arXiv.1905.01614.

[63] M. D. Hossain and D. Chen, "Segmentation for Object-Based Image Analysis (OBIA): A review of algorithms and challenges from remote sensing perspective," *ISPRS Journal of Photogrammetry and Remote*

Sensing, vol. 150, pp. 115-134, 2019, doi: 10.1016/j.isprsjprs.2019.02.009.

[64] H. Costa, G. M. Foody, and D. S. Boyd, "Supervised methods of image segmentation accuracy assessment in land cover mapping," *Remote Sensing of Environment*, vol. 205, pp. 338-351, 2018, doi: 10.1016/j.rse.2017.11.024.

[65] Y. Xiao, L. Daniel, and M. Gashinova, "Image segmentation and region classification in automotive high-resolution radar imagery," *IEEE Sensors Journal*, vol. 21, no. 5, pp. 6698-6711, 2020, doi: 10.1109/JSEN.2020.3043586.

[66] M. Z. Alom, C. Yakopcic, M. Hasan, T. M. Taha, and V. K. Asari, "Recurrent residual U-Net for medical image segmentation," *Journal of Medical Imaging*, vol. 6, no. 1, pp. 014006-014006, 2019, doi: 10.1117/1.JMI.6.1.014006.

[67] N. Siddique, S. Paheding, C. P. Elkin, and V. Devabhaktuni, "U-net and its variants for medical image segmentation: A review of theory and applications," *IEEE Access*, vol. 9, pp. 82031-82057, 2021, doi: 10.1109/ACCESS.2021.3086020.

[68] M. H. Hesamian, W. Jia, X. He, and P. Kennedy, "Deep learning techniques for medical image segmentation: achievements and challenges," *Journal of digital imaging*, vol. 32, pp. 582-596, 2019, doi: 10.1007/s10278-019-00227-x.

[69] A. Sinha and J. Dolz, "Multi-scale self-guided attention for medical image segmentation," *IEEE Journal of Biomedical and Health Informatics*, vol. 25, no. 1, pp. 121-130, 2021, doi: 10.48550/arXiv.1906.02849.

[70] F. Shi *et al*., "Review of artificial intelligence techniques in imaging data acquisition, segmentation, and diagnosis for COVID-19," *IEEE Reviews in Biomedical Engineering*, vol. 14, pp. 4-15, 2021, doi: 10.1109/RBME.2020.2987975.

[71] F. Munawar, S. Azmat, T. Iqbal, C. Grönlund, and H. Ali, "Segmentation of lungs in chest X-ray image using generative adversarial networks," *IEEE Access*, vol. 8, pp. 153535-153545, 2020, doi: 10.1109/ACCESS.2020.3017915.

[72] S. Wang, D. M. Yang, R. Rong, X. Zhan, and G. Xiao, "Pathology image analysis using segmentation deep learning algorithms," *The American Journal of Pathology*, vol. 189, no. 9, pp. 1686-1698, 2019, doi: 10.1016/j.ajpath.2019.05.007.

[73] S. M. Anwar, M. Majid, A. Qayyum, M. Awais, M. Alnowami, and M. K. Khan, "Medical image analysis using convolutional neural networks: a review," *Journal of Medical Systems*, vol. 42, pp. 1-13, 2018, doi: 10.1007/s10916-018-1088-1.

[74] Y. Lu, W. Ma, X. Dong, M. Brown, T. Lu, and W. Gan, "Differentiate Xp11.2 Translocation Renal Cell Carcinoma from Computed Tomography Images and Clinical Data with ResNet-18 CNN and XGBoost," *CMES - Computer Modeling in Engineering & Sciences*, vol. 136, no. 1, 2023, doi: 10.32604/cmes.2023.024909.

[75] V. Narayan, P. K. Mall, A. Alkhayyat, K. Abhishek, S. Kumar, and P. Pandey, "[Retracted] Enhance-Net: An Approach to Boost the Performance of Deep Learning Model Based on Real-Time Medical Images," *Journal of Sensors*, vol. 2023, no. 1, p. 8276738, 2023, doi: 10.1155/2023/8276738.

[76] S. A. El-Feshawy, W. Saad, M. Shokair, and M. Dessouky, "IoT framework for brain tumor detection based on optimized modified ResNet 18 (OMRES)," *The Journal of Supercomputing*, vol. 79, no. 1, pp. 1081-1110, 2023, doi: 10.1007/s11227-022-04678-y.

[77] P. Chotikunnan, T. Puttasakul, R. Chotikunnan, B. Panomruttanarug, M. Sangworasil, and A. Srisiriwat, "Evaluation of single and dual image object detection through image segmentation using ResNet18 in robotic vision applications," *Journal of Robotics and Control (JRC)*, vol. 4, no. 3, pp. 263-277, 2023, doi: 10.18196/jrc.v4i3.17932.

[78] R. BME, *Anonymized CT DICOM Dataset Compilation for Research Purposes*. Zenodo, 2016, doi: 10.5281/zenodo.152448.